



# A Morphological Study of Two Young Multipolar Planetary Nebulae

Shi-Bo Wen<sup>1</sup>, Chih-Hao Hsia<sup>2</sup> , Xiao-Xi Kang<sup>3,4</sup>, Rui Chen<sup>1</sup>, and Tao Luo<sup>5,6</sup>

<sup>1</sup> State Key Laboratory of Lunar and Planetary Sciences, Macau University of Science and Technology, Macau, China

<sup>2</sup> The Laboratory for Space Research, Faculty of Science, The University of Hong Kong, Cyberport 4, Hong Kong, China; [xiazh.tw@yahoo.com.tw](mailto:xiazh.tw@yahoo.com.tw), [xiazh@hku.hk](mailto:xiazh@hku.hk)

<sup>3</sup> Deep Space Exploration Laboratory, Beijing 100043, China

<sup>4</sup> Lunar Exploration and Space Engineering Center, China National Space Administration, Beijing 100190, China

<sup>5</sup> Shien-Ming Wu School of Intelligent Engineering, South China University of Technology, Guangzhou 511442, China

<sup>6</sup> Zhuhai Bojay Electronics Co., Ltd., Zhuhai 519075, China

Received 2022 October 27; revised 2023 January 16; accepted 2023 February 20; published 2023 March 10

## Abstract

We carry out an optical morphological and infrared spectral study for two young planetary nebulae (PNs) Hen 2-158 and Pe 1-1 to understand their complex shapes and dust properties. Hubble Space Telescope optical images reveal that these nebulae have several bipolar-lobed structures and a faint arc with a clear boundary is located at the northwestern side of Pe 1-1. The presence of this arc-shaped structure suggests that the object interacts with its nearby interstellar medium. Spitzer IRS spectroscopic observations of these young nebulae clearly show prominent unidentified infrared emission features and a weak silicate band in Pe 1-1, indicating that Hen 2-158 is a carbon-rich nebula and Pe 1-1 has a mixed chemistry dust environment. Furthermore, we construct two three-dimensional models for these PNs to realize their intrinsic structures. The simulated models of the nebulae suggest that multipolar nebulae may be more numerous than we thought. Our analyses of spectral energy distributions for Hen 2-158 and Pe 1-1 show that they have low luminosities and low stellar effective temperatures, suggesting that these nebulae are young PNs. A possible correlation between typical multipolar young PNs and nested nebulae is also discussed.

**Key words:** ISM: structure – (ISM:) planetary nebulae: individual (Hen 2-158, Pe 1-1) – stars: AGB and post-AGB – infrared: ISM

## 1. Introduction

Planetary nebulae (PNs) are generally considered to be the end-products of intermediate- to low-mass stars. Although their lifetimes are very short ( $\sim 10^4$  yr) compared to the entire lifetimes of the stars, they occur for a large proportion of the stellar population, and therefore we can study galactic dynamics through these objects (Chabrier 2003; Parker et al. 2017). Similarly, PNs are also well suited as probes of galactic evolution. During the asymptotic giant branch (AGB) phase of PN progenitors, materials produced from the core regions are mixed with outer shells and then blown into their surrounding interstellar medium (ISM). When the nebular shells of PNs are ionized by ultraviolet (UV) photons emitted from their central stars (CSs), the distinct fine-structure lines ([O III], [N II], and [S II]) are thus produced. The prominent features are relatively clear compared to the continua of central sources, and therefore these emission lines provide an effective tool for probing galactic properties and stellar elemental abundances (Kwok 2000; Delgado-Inglada 2017). With the help of some physical parameters of PNs (such as radial velocities, luminosities, and temperatures), we can also study the kinematic properties and mass distributions of these objects (Merrett et al. 2006; Herrmann et al. 2008; Coccato et al. 2009).

PNs are traditionally known for their spherical shells. However, with the developments of CCD imaging and the advancement of observational techniques, only about 20% of all discovered PNs are found to be spherically symmetric (Jacoby et al. 2001). In the young planetary nebula (YPN) stage, these nebulae usually exhibit a multiple-lobed shape or have at least two pairs of axisymmetric structures such as NGC 6644 (Hsia et al. 2010), H 1-54, Hen 2-447, Hen 2-86, IC 5117, and M 1-30 (Hsia et al. 2014), which differ in shape from AGB stars and evolved PNs. In addition, some microstructures involving ISM interactions (jets, equatorial tori, two-dimensional rings, extended halos, ansae, and knots) can also be seen around these objects. The appearance of young multipolar PNs suggests a possible correlation between the shapes of these nebulae and their central sources (Hsia et al. 2014, 2019). Although there have been some discussions on the nature and formation of young multipolar PNs, the exact physical mechanisms leading to these structures are still unclear.

Hen 2-158 (PN G327.8-06.1) was originally discovered in an  $H\alpha$  imaging survey and later confirmed by spectroscopic observations (Henize 1967). This nebula has an angular diameter of  $\sim 3''.4 \times 2''.9$  in  $H\alpha$  emission (Tylenda et al. 2003). To understand the relationship between the properties of

**Table 1**  
Summary of HST WFC3 Imaging Observations

Object	R.A. (J2000.0)	Decl. (J2000.0)	Filter	Exposures (s)	Observation Date	Program ID
Pe 1-1	10:38:27.59	−56:47:07.2	F502N	300 × 2	2009 Oct 05	11657
			F200LP	16, 120	2009 Oct 05	11 657
			F350LP	16, 120	2009 Oct 05	11 657
Hen 2-158	16:23:30.65	−58:19:22.8	F502N	300 × 2	2010 Aug 21	11657
			F200LP	2, 20	2010 Aug 21	11 657
			F350LP	2, 20	2010 Aug 21	11 657

the CS and those of its surrounding nebula for this object, Moreno-Ibáñez et al. (2016) derived the mass and luminosity of its CS of  $\sim 0.567 M_{\odot}$  and  $2200 L_{\odot}$ , adopting a distance to the PN of 15 kpc. The nebula Pe 1-1 (PN G285.4+01.5) was first discovered and identified as a PN by Perek (1960). Based on a series of spectroscopic observations, Burlak & Kniazev (2013) determined abundances of seven elements (Ar, Cl, He, N, Ne, O, and S) and physical parameters of the source to understand its nebular properties. Peña et al. (2017) analyzed the kinematics of this nebula and then estimated its evolutionary age of about 3495 yr. Danehkar (2022) performed a kinematic study for Pe 1-1 and found the collimated outflows by using the integral-field-unit (IFU) spectrograms. Although these two nebulae have been reported in a few times in the literature, we still know very little about them.

To further understand the nebular structures and properties of the young PNs, we study the optical images and infrared (IR) spectra of these two nebulae (Hen 2-158 and Pe 1-1) through Hubble Space Telescope (HST) and Spitzer Space Telescope observations, respectively. The two young PNs both show a multipolar appearance. In Section 2, we describe the optical and IR measurements and corresponding data reductions. The optical imaging and IR spectroscopic results for these PNs are given in Section 3. The property analyses of these nebulae by using the spectral energy distributions (SEDs) are presented in Section 4. A comparison of three-dimensional (3D) models and observation results of these nebulae are presented in Section 5. A possible correlation between typical multipolar YPNs and nested nebulae is discussed in Section 6. The final conclusion is summarized in Section 7.

## 2. Observations and Data Reduction

### 2.1. HST Optical Imaging

All high-resolution HST optical imaging observations are obtained from the Mikulski Archive for Space Telescopes (MAST) and observed with the Wide Field Camera 3 (WFC3) instrument through the program 11657 (PI: L. Stanghellini). The WFC3 supplies a  $2'.7 \times 2'.7$  field-of-view (FOV) imaging with an image resolution of  $0''.04 \text{ pixel}^{-1}$ . All nebulae are mapped with two broad-band and one narrow-band filters: F350LP ( $\lambda_c = 5812 \text{ \AA}$ ,  $\Delta\lambda = 4840 \text{ \AA}$ ), F200LP ( $\lambda_c = 4895 \text{ \AA}$ ,

$\Delta\lambda = 5680 \text{ \AA}$ ), and F502N [O III] ( $\lambda_c = 5012 \text{ \AA}$ ,  $\Delta\lambda = 65 \text{ \AA}$ ), respectively. Total exposure times for these nebulae are set to be from 22 to 600 s. We process and calibrate all images through IRAF STSDAS package procedures. Successful flat-field subtraction, bias calibration, and cosmic-rays removal are performed. A journal of HST WFC3 imaging observations is summarized in Table 1. Processed color-composite and F350LP images of the two young PNs Pe 1-1 and Hen 2-158 are shown in Figures 1 and 2.

### 2.2. Spitzer IRS Spectra

The Infrared Spectrograph (IRS) is a spectroscopic instrument mounted on Spitzer Space Telescope. The IRS observations of Hen 2-158 and Pe 1-1 were obtained between 2008 August 16 and 2008 October 07 through the program 50261 (PI: L. Stanghellini). Observations of these nebulae were made with the Long-Low (LL), Short-High (SH), and Short-Low (SL) modules, which cover a spectral range of  $5.2\text{--}19.6 \mu\text{m}$  with spectral dispersions ranging from 57 to 600. The slit sizes are  $10''.5 \times 168''$ ,  $4''.7 \times 11''.3$ , and  $3''.6 \times 57''$  for the LL, SH, and SL modules, respectively, and the exposure times range from 40 to 80 s. The slits of all IRS observations are set through the central parts of the two nebulae.

We start to reduce and calibrate the basic data of IRS spectra for these nebulae using the version s18.7 of Spitzer Science Center (SSC) pipeline. The rogue-pixel removal is performed through the IRSCLEAN program and then the SMART package (Higdon et al. 2004) is employed to extract the spectral measurements. To obtain high-quality infrared spectra of these objects, the final spectrum of each nebula is made via combining the IRS observations with various exposures.

Comparing the IRS measurements in the LL and SH modules, we note that the slit size of SL observations ( $3''.6 \times 57''$ ) is smaller than those of LL ( $10''.5 \times 168''$ ) and SH ( $4''.7 \times 11''.3$ ) observations, leading to intensity losses due to the smaller SL aperture size. Therefore, scaling corrections for SL measurements of these PNs are needed. In order to match the continuum fluxes in the overlapping regions of SH/LL and SL measurements, we scaled the SL parts of two nebulae by factors of 1.13 for Hen 2-158 and 1.08 for Pe 1-1, respectively. A journal of IRS observations for these YPNs is summarized in Table 2.

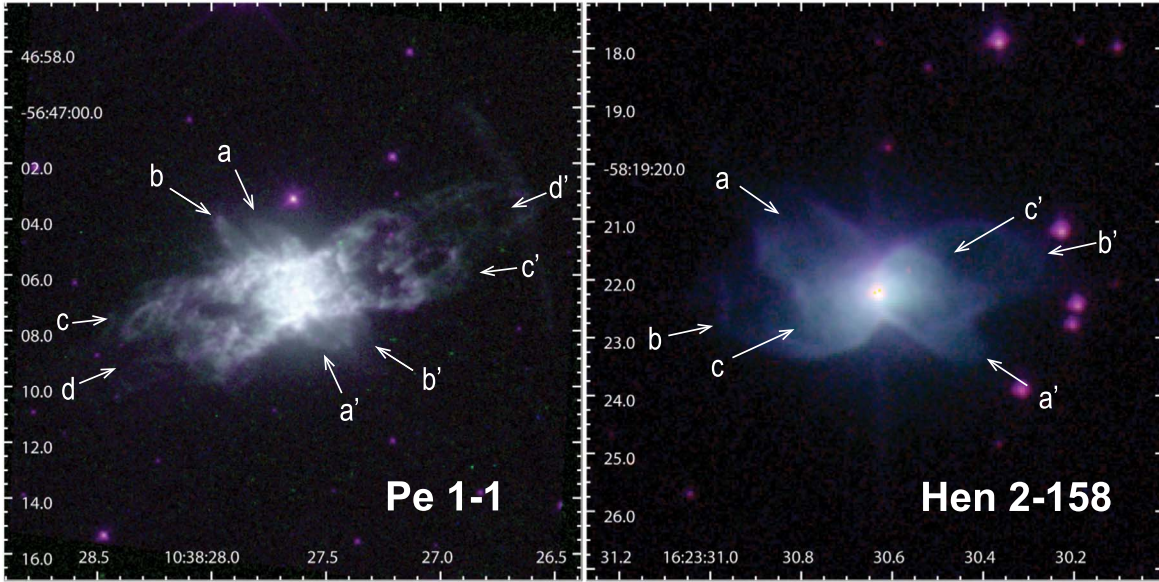


**Figure 1.** HST color-composite images of Pe 1-1 (left) and Hen 2-158 (right) shown on logarithmic scales. These nebulae are made from three filters: F350LP (shown as red), [O III] (green), and F200LP (blue). Various morphological features and several pairs of bipolar lobes are marked.

### 3. Results

#### 3.1. Imaging Morphology

##### 3.1.1. Multipolar Young Planetary Nebula—Hen 2-158

Quireza et al. (2007) first classified this nebula as a Peimbert-type III PN according to its nebular abundances and galactic parameters. By examining the deep HST optical image of Hen 2-158, it is clear that this object shows a multipolar appearance extending along east–west direction and consisting of three pairs of lobes (labeled as lobes  $a - a'$ ,  $b - b'$ , and  $c - c'$ ) as shown in the right panel of Figure 1. These lobes with a clear edge roughly intersect at the center of this PN, which shows a similar appearance to the young PN Hen 2-447 reported in a previous study (Hsia et al. 2014). The orientations and dimensions of these lobe-like features are obtained by fitting their shapes to the HST images. The position angles (PAs) of three bipolar-lobed features ( $a - a'$ ,  $b - b'$ , and  $c - c'$ ) are  $PA = 58^\circ \pm 3^\circ$ ,  $105^\circ \pm 4^\circ$  and  $113^\circ \pm 3^\circ$ , respectively, and their corresponding angular sizes are  $4''.44 \times 0''.88$ ,  $5''.55 \times 1''.24$  and  $2''.24 \times 1''.17$ . These measurements are summarized in Table 3. Assuming a mean PN expansion velocity of  $22.5 \text{ km s}^{-1}$  measured from [N II] line (Weinberger 1989) and a distance of 6.1 kpc for Hen 2-158 (Tajitsu & Tamura 1998), the physical size for lobe  $b - b'$  is  $0.166 \text{ sec } \theta \text{ pc}$  ( $\theta$  represents the tilt angle), then the dynamical age is about  $3550 \text{ sec } \theta \text{ yr}$ . This result suggests that Hen 2-158 is a young nebula. The deduced dynamical age of this object is a rough estimate because its projected size involves the uncertain inclination angle and an assumed expansion velocity.

##### 3.1.2. Multipolar Young Planetary Nebula Pe 1-1 and its Surrounding Arc-like Structure

Previously, Sahai et al. (2011) classified Pe 1-1 as a bipolar PN with closed-end lobe features and this PN has a [WC5] type central source (Weidmann et al. 2020). The deep HST image (see the left panel of Figure 1) reveals that the nebula elongates roughly along the northwest–southeast direction and exhibits a multi-lobed shape with an angular size of  $\sim 16''.6 \times 5''.4$ , which is larger than previously measured ( $9''.6 \times 5''.9$ , Stanghellini et al. 2016). From Figures 1 and 2, the main nebula of PN Pe 1-1 clearly shows a multipolar appearance similar to that of M 1-59 and M 1-61 (Hsia et al. 2014) and contains four bipolar lobes with different orientations (marked as  $d - d'$ ,  $c - c'$ ,  $b - b'$ , and  $a - a'$ ) intersected in the central part. These structures may be the results of the collimated outflows ejected along various directions and/or their directions changing due to the precessions of the rotation axes of central sources or binary interactions in the nuclei of these objects during the ending of AGB phase or post-AGB stage (Hsia et al. 2014). To measure the PAs and sizes of these four bipolar features, we fit ellipses to these structures. The best-fit orientations and sizes of these features are given in Table 3. Assuming an expansion velocity of  $23 \text{ km s}^{-1}$  for Pe 1-1 and a tilt angle of  $15^\circ$  for lobe  $d - d'$  (Danekar 2022), and adopting a distance of 4.16 kpc (Phillips 2004), the dynamical age of this compact PN is derived to be  $\sim 2030 \text{ yr}$ , which suggests that this object is quite young (Sahai et al. 2011; Peña et al. 2017).

From Figure 2, a faint arc-shaped feature with a radius of  $\sim 8''.7$  around Pe 1-1 is also visible in the HST image. This

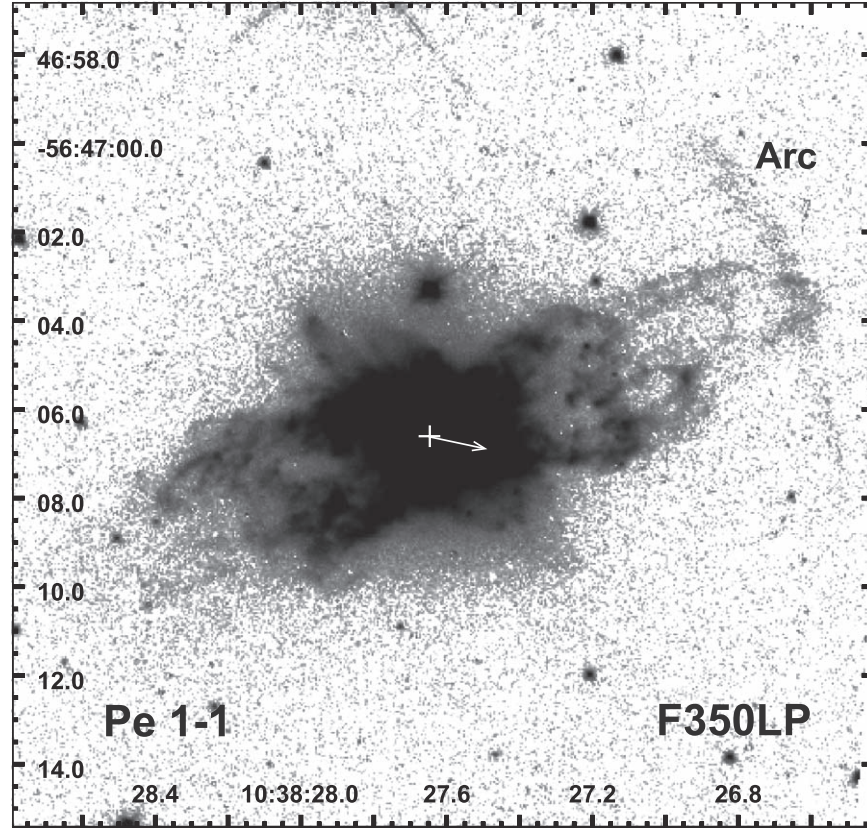


**Figure 2.** Multipolar structures of PN Pe 1-1 are displayed in gray HST F350LP image shown with a logarithmic scale to better reveal outer features. A faint arc-like filament located at the northwest and west parts of the object is visible in this deep image. The white arrow and cross represent the proper motion direction of the nebula and the position of the central source, respectively.

**Table 2**  
Available Spitzer IRS Spectroscopic Observations

Name	ID	Observation Date	Wavelength Range ( $\mu\text{m}$ )	Exposures (s)	S/N
Pe 1-1	AOR key 25 851 392	2008 Aug 16	5.2–14.5 (SL)	$20 \times 4$	>21
			9.9–19.6 (SH)	$20 \times 2$	>38
Hen 2-158	AOR key 25 856 512	2008 Oct 7	5.2–14.5 (SL)	$20 \times 4$	>18
			14.0–21.7 (LL)	$20 \times 2$	>25

filament-like arc shown with a clear edge is located at the northwest and west parts (from  $\text{PA} = -41^\circ$  to  $-95^\circ$ ) of the PN, which indicates that this object is interacting with its surrounding ISM (Wareing et al. 2007; Ramos-Larios et al. 2018; Hsia et al. 2020). The direction of proper motion of Pe 1-1 is calculated as  $\text{PA} = -102^\circ$  (Marocco et al. 2021), which approximately corresponds to the position of this bow-shocked filament. The presence of this filamentary structure may provide evidence that this PN moves through its surrounding high-density ISM (Dgani & Soker 1998; Ali et al. 2012), which agrees with recent result suggested by Danehkar (2022).

Furthermore, the averaged intensity surface-brightness (SB) profile of this arc-shaped structure in the HST F350LP band is plotted in Figure 3. The plot is made from the averaged intensity of the regions between  $\text{PA} = -41^\circ$  and  $-95^\circ$  with an interval of  $3^\circ$ , after excluding all stars in the image. In this profile, we can see that the peak SB intensities of arc-filament feature ( $\sim 8''$  to the center) and lobe structure ( $\sim 4''$  to the central source) are about  $4.8 \times 10^{-3}$  and  $1.1 \times 10^{-2}$  times lower than that of central bright nebula, respectively. The filamentary arc also shows a brightness similar to typical AGB halo (approximately equal to  $10^{-3}$  SB of main nebula; Corradi et al. 2003). If we assume that

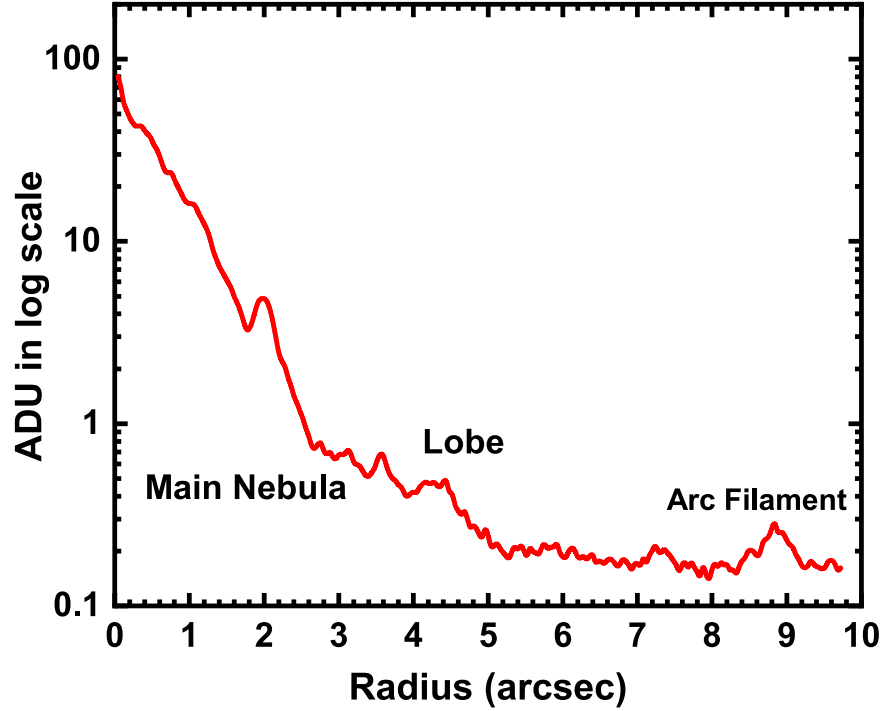


**Figure 3.** Averaged surface-brightness profile of PN Pe 1-1 in the HST F350LP band made between PA =  $-41^\circ$  and PA =  $-95^\circ$  except for some regions dominated by the lobe  $d - d'$ . The  $x$ -axis represents the distance to central source with the unit of arcsecond. The positions of main nebula and arc-like filament are also marked.

**Table 3**  
Observed Parameters of Lobe-like Features for Hen 2-158 and Pe 1-1

Feature	Hen 2-158		Pe 1-1		Inclination <sup>c</sup> ( $^\circ$ )
	P.A. <sup>a</sup> ( $^\circ$ )	Size <sup>b</sup> ( $l'' \times w''$ )	P.A. <sup>a</sup> ( $^\circ$ )	Size <sup>b</sup> ( $l'' \times w''$ )	
Lobe $a - a'$	$58 \pm 3$	$4.44 \times 0.88$	$34 \pm 4$	$5.68 \times 0.75$	...
Lobe $b - b'$	$105 \pm 4$	$5.51 \times 1.24$	$48 \pm 2$	$6.77 \times 0.77$	...
Lobe $c - c'$	$113 \pm 3$	$2.24 \times 1.17$	$101 \pm 3$	$12.72 \times 2.55$	...
Lobe $d - d'$	...	...	$112 \pm 4$	$17.62 \times 3.13$	$15^d$

**Notes.**

<sup>a</sup> Estimated from the orientations of major axes.

<sup>b</sup> Measured from HST F350LP images.

<sup>c</sup> Adopting the orientation of the sky plane being  $0^\circ$  (referred to the plane of the sky).

<sup>d</sup> Adopted from Danekkar (2022), the orientation angle of the sky plane being  $0^\circ$ .

the distance to this PN is  $4.16 \pm 0.18$  kpc (Phillips 2004) and a mean AGB expansion velocity for the arc-shaped filament is  $13.9 \text{ km s}^{-1}$  (Gussie & Taylor 1994), the dynamical age of this faint feature is about  $17,400 \pm 750$  yr, suggesting that the filamentary arc erupts in the AGB stage.

### 3.2. Infrared Spectral Properties of Hen 2-158 and Pe 1-1

To study the dust chemical compositions and surrounding environments of these nebulae, we have implemented mid-IR

spectroscopic measurements aimed at the two objects (Hen 2-158 and Pe 1-1) for examining the existences of unidentified infrared emission (UIE) bands and/or silicate features. In these IRS observations, the arc-like filament around Pe 1-1 shown in Figure 3 is not detected probably because this structure can be only seen in the visible or/and it shows low surface brightness. By subtracting the continua of these two YPNs fitted with cubic polynomials, we obtained their continua-subtracted spectra from these actual measurements to highlight weaker features. Figures 4 and 5 show the residual IRS spectra of Hen 2-158 and Pe 1-1, respectively. From Figures 4 and 5, the continua-

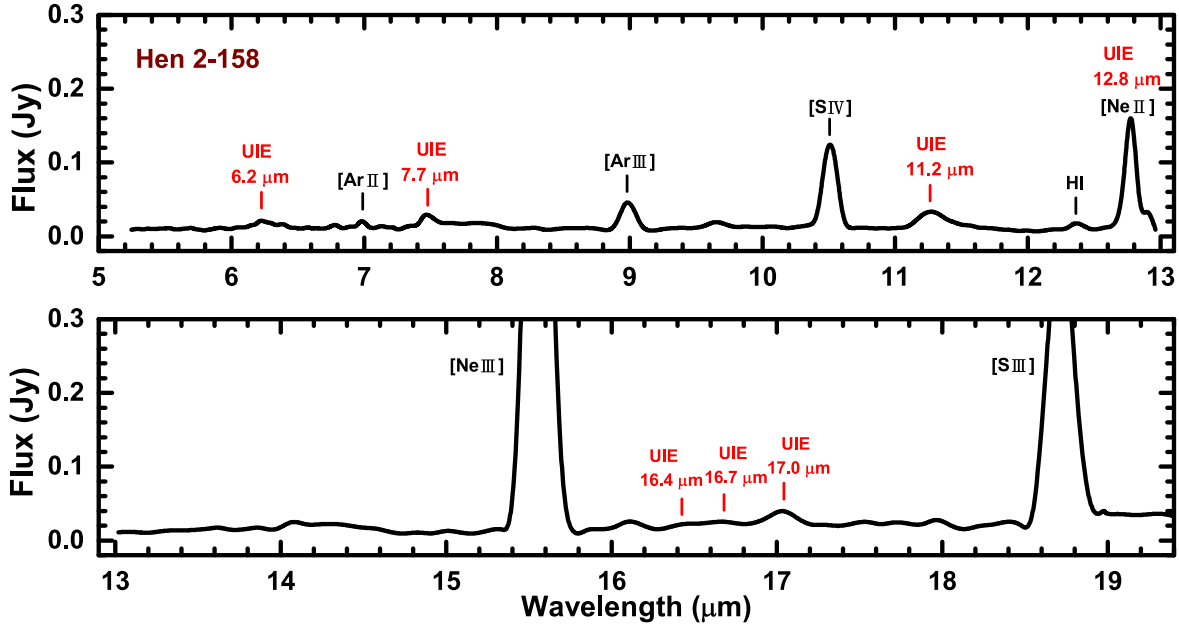


**Figure 4.** Spitzer IRS continua-subtracted spectra of Hen 2-158 with the spectral coverage from 5 to 19.4  $\mu\text{m}$ . Strong forbidden lines, H I line, and known UIE bands are marked.

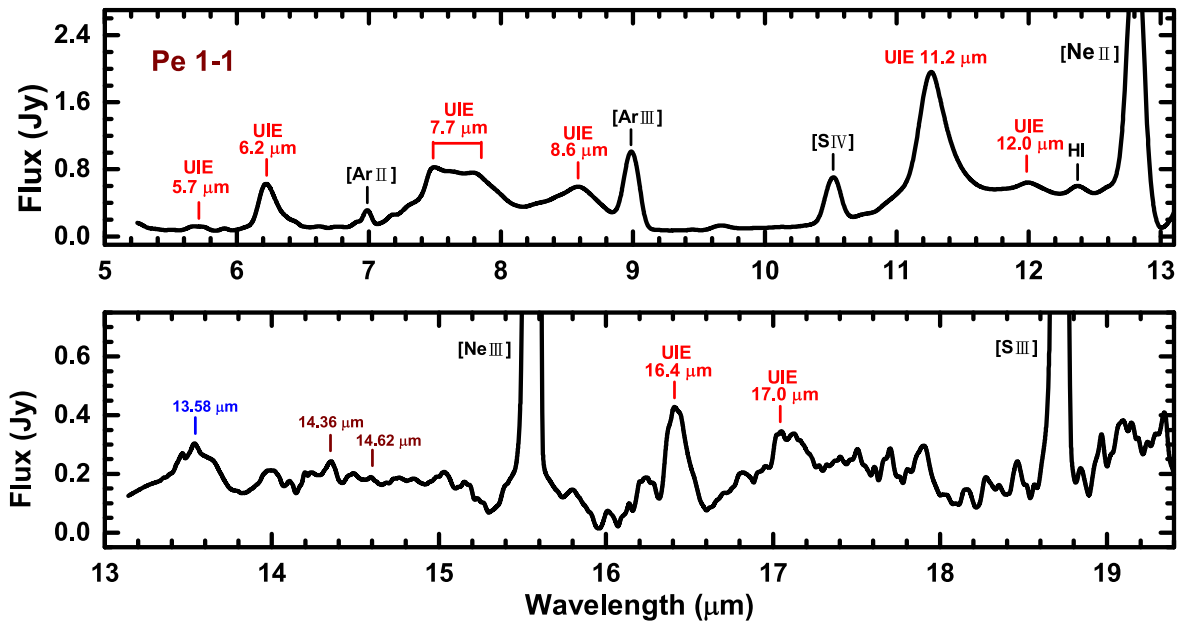


**Figure 5.** Continua-subtracted spectral measurements of Pe 1-1 for a wavelength range from 5 to 19.4  $\mu\text{m}$ . The prominent emission features, H I line, and known UIE bands are marked. Blue and brown lines denote the positions of crystalline silicate and new identified UIE features (Hsia et al. 2021), respectively.

subtracted spectra of these nebulae are mainly dominated by strong emission lines such as [Ar II] at 6.99  $\mu\text{m}$ , [Ar III] at 8.99  $\mu\text{m}$ , [Ne II] at 12.81  $\mu\text{m}$ , [Ne III] at 15.56  $\mu\text{m}$ , [S IV] at 10.51  $\mu\text{m}$ , and weak H I line at 12.37  $\mu\text{m}$ , which are commonly seen in the typical YPN spectra.

Apart from strong fine-structure lines, some known UIE bands at 6.2, 7.7, 8.6, 11.2, 12.0, 12.8, 16.4, 16.7, and 17.0  $\mu\text{m}$  can be seen in their IRS spectra. Furthermore, a weak crystalline silicate feature at 13.58  $\mu\text{m}$  (Molster et al. 2002) and two newly identified bands at 14.36 and 14.62  $\mu\text{m}$

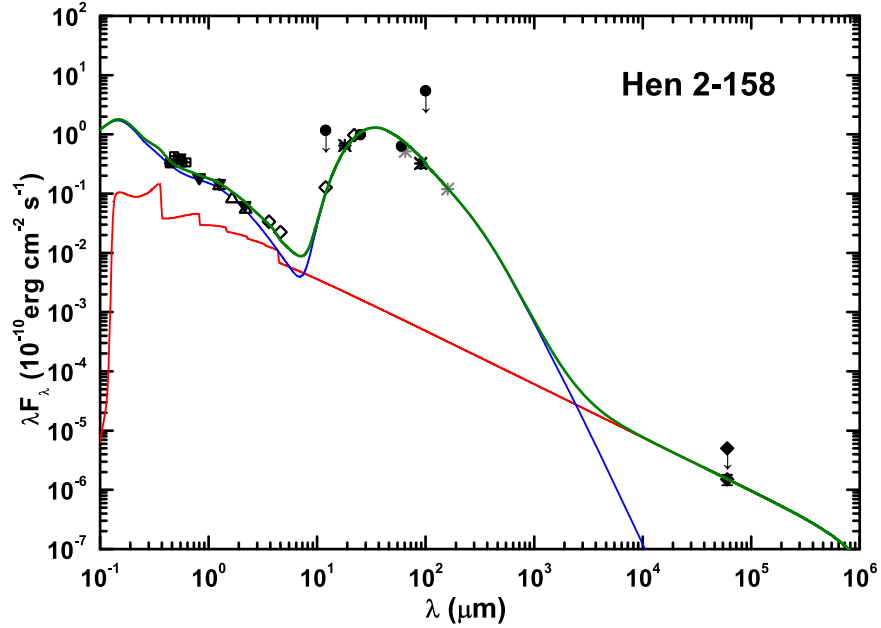


**Figure 6.** Composite SED of Hen 2-158 from the radio to the UV. Sloan  $g'$ ,  $r'$ , and  $i'$  photometry are shown as open squares, the  $V$  and  $B$  measurements as filled squares, the 2MASS photometry as open triangles, DENIS results as filled triangles, WISE photometric results as open diamonds, MSX measurements as open circles, IRAS results as filled circles, AKARI measurements as asterisks, and available radio detections as filled diamonds. Light asterisks show the uncertain AKARI measurements and the IRAS detections at 100 and 12  $\mu\text{m}$  are upper limit measurements. The red and blue curves denote the nebular-continuum contribution and the dust emission estimated by using the radiation-transfer simulation. Total fluxes originated from these components are plotted as a green line.

(Hsia et al. 2021) are detected in Pe 1-1. These features are first discovered in the two nebulae and reveal a carbon-rich dust characteristic in Hen 2-158 and a mixed chemistry dust environment in Pe 1-1, which may dabble in carbon-rich dust mass-loss processes originated from the massive progenitors of YPNs (Stanghellini et al. 2012) such as IRAS 21 282+5050 and NGC 6644 (Hsia et al. 2010, 2019). Further detailed infrared imaging observations together with high-resolution spectroscopic measurements are needed to study the spatial distributions of UIE bands.

#### 4. Spectral Energy Distribution

The SED as a collection of multi-band observations provides a useful tool for us to understand the natures and physical properties of studied nebulae. In order to better estimate the relative contents of dust, photospheric, and nebular constituents, we made two individual SEDs with wavelength coverage from ultraviolet (UV) to the radio for Hen 2-158 and Pe 1-1 (Figures 6 and 7). The visual  $V$  and  $B$  magnitudes and Sloan  $i'$ ,  $r'$ , and  $g'$  photometric data of the young nebulae are taken from Henden et al. (2016). Mid- and near-IR photometry are obtained from AKARI, Midcourse Space Experiment (MSX), Infrared Astronomical Satellite (IRAS), Two Micron All Sky Survey (2MASS), and Deep Near-Infrared Southern Sky Survey (DENIS) source catalogs, respectively. Additionally,

we included some photometric measurements from Wide-field Infrared Survey Explorer (WISE) images using the same methods described in Hsia & Zhang (2014). Color calibrations for observed WISE bands at 22, 12, 4.6, and 3.4  $\mu\text{m}$  are performed using the correction coefficients given in Wright et al. (2010). These photometric results are summarized in Table 4.

From Figures 6 and 7, we can see that the main contributions of these nebulae in fluxes are mostly from the dust components with IR continua. In the SED constructed, the total radiation fluxes emitted from these two PNs are fitted with a two-component model consisting of dust emission and reddened photospheric continuum (originated from nebular and central source emission) using the same methods as described in Hsia et al. (2019). These SEDs clearly reveal relative fractions of individual components of the nebulae (Figures 6 and 7). For the dust continua with the range from 10 to 1000  $\mu\text{m}$  seen in the SEDs, we find that the distributions of these components are too wide to be fitted well using a dust blackbody only, and thus we adopted the DUSTY radiation transfer code (Ivezic et al. 1999) for fitting the observable curves of these two nebulae. In the fitting, we assumed that the compositions of dust particles are graphite-silicate mixtures and the particle sizes with standard MRN distributions (Mathis et al. 1977) are adopted for Hen 2-158 and Pe 1-1. Although the adopted parameters do not represent the actual states of two young PNs well, these

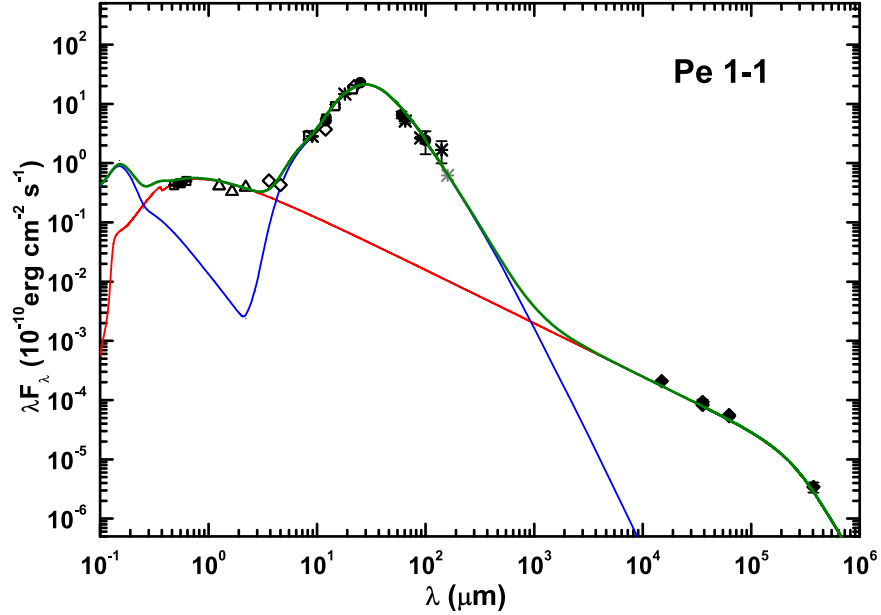


**Figure 7.** Composite SED of PN Pe 1-1 with the wavelength range from  $10^{-1}$  to  $10^6 \mu\text{m}$ . The notations of model fittings and the symbols of photometric points are the same as Figure 6.

values can still give approximate results to fit the observed SED curves.

According to our best-fit results, the closest estimates for color temperatures of central sources are  $32,000 \pm 3000 \text{ K}$  and  $83,000 \pm 4000 \text{ K}$  for the studied PNs of Hen 2-158 and Pe 1-1, respectively, these derived values are roughly the same as earlier conclusions of  $30,200 \pm 170 \text{ K}$  (Moreno-Ibáñez et al. 2016) for Hen 2-158 and  $85,000 \text{ K}$  (Acker et al. 2002) for Pe 1-1. If we adopted the distances to Hen 2-158 and Pe 1-1 of  $6.1 \text{ kpc}$  (Tajitsu & Tamura 1998) and  $4.16 \text{ kpc}$  (Phillips 2004), respectively, the entire luminosities of these PNs are about  $602 L_{\odot}$  for Hen 2-158 and  $2160 L_{\odot}$  for Pe 1-1. Given such low luminosities and effective temperatures of the exciting stars of these two nebulae, the locations of these PNs on the Hertzsprung-Russell diagram indicate that they are quite young, in agreement with previous results (Sahai et al. 2011; Stanghellini et al. 2016).

## 5. Simulating 3D Structures of Hen 2-158 and Pe 1-1

According to the results presented in Sections 3.1.2 and 3.1.1, it is clear that Hen 2-158 and Pe 1-1 are compact YPNs with multiple lobes. To further study and understand their complex structures more intuitively, we use a *SHAPE X* software program (Steffen et al. 2011) to construct 3D models of these two objects. *SHAPE X* is a modern interactive 3D modeling technique that allows us to manipulate in a way to establish astrophysical processes and their parameters, construct morphological modeling, and visualize the 3D structures of studied nebulae with a polygonal grid form. The sizes and orientations of simulated lobes of each nebula are constrained

by the observed HST images (see Table 3), and the surface brightnesses of ionized structures ( $\int n_e^2 d\ell$ ) are adopted using the parameters presented in Hsia et al. (2014). We do not consider any excitation effect, hydrodynamic simulation, and radiative transfer process in these models because our primary purpose is to understand the 3D spatial structures of these PNs and then compare their 2D projected appearances mapped onto the sky plane with observed HST results.

Our models are simulated according to the observed multiple lobes of two nebulae shown in the HST images, where Hen 2-158 reveals three bipolar-lobed features and Pe 1-1 has four pairs of expanding structures that close at their tips (see Figure 8). We note that some lobes of these two YPNs reveal a shell-like appearance, therefore an assumed thin-shell thickness of  $0.2$  is applied for these structures. Although we cannot make good estimates for the lobe sizes of these YPNs due to the lack of high-resolution and high-dispersion spectroscopic observations, the previous studies have shown that the lobe lengths of some multipolar nebulae are roughly equal (Guerrero & Manchado 1998; Santander-García et al. 2010; Rubio et al. 2015). In the absence of the kinematic data of nebular structures for these two objects, it is reasonable to assume that the lobes of each nebula are of equal size. Taking Hen 2-158 as an example, assuming that these three bipolar lobes all have the same length and lobe  $b - b'$  is parallel to the sky plane ( $\theta = 90^\circ$  referred to the line of sight), the inclination angles of lobes  $a - a'$  and  $c - c'$  are derived to be  $36^\circ$  and  $66^\circ$ , respectively. Similarly, given the lobe  $d - d'$  as a pair of prominent lobes with a tilt angle of  $15^\circ$  (referred to the sky plane) for Pe 1-1 (Danekar 2022), we deduce that the inclination angles of lobes

**Table 4**  
Photometric Measurements of Hen 2-158 and Pe 1-1

Filters	Hen 2-158		Pe 1-1	
	Flux/Flux density	References	Flux/Flux density	References
Central Star and Nebula				
<i>B</i> (mag)	14.906 ± 0.012	Henden et al. (2016)	...	...
<i>V</i> (mag)	14.250 ± 0.20	Henden et al. (2016)	14.178 ± 0.037	Henden et al. (2016)
Sloan <i>g'</i> (mag)	14.166 ± 0.011	Henden et al. (2016)	14.397 ± 0.029	Henden et al. (2016)
Sloan <i>r'</i> (mag)	14.117 ± 0.131	Henden et al. (2016)	13.843 ± 0.048	Henden et al. (2016)
Sloan <i>i'</i> (mag)	...	...	14.301 ± 0.053	Henden et al. (2016)
Dust <sup>a</sup>				
2MASS <i>J</i> (mag)	13.663 ± 0.036	Cutri et al. (2003)	12.457 ± 0.045	Cutri et al. (2003)
2MASS <i>H</i> (mag)	13.594 ± 0.048	Cutri et al. (2003)	12.065 ± 0.042	Cutri et al. (2003)
2MASS <i>Ks</i> (mag)	13.067 ± 0.040	Cutri et al. (2003)	10.931 ± 0.034	Cutri et al. (2003)
DENIS <i>I</i> (mag)	14.202 ± 0.030	DENIS database	...	...
DENIS <i>J</i> (mag)	13.635 ± 0.100	DENIS database	...	...
DENIS <i>K</i> (mag)	12.889 ± 0.140	DENIS database	...	...
WISE 3.4 μm (mag)	12.161 ± 0.024	this study	9.317 ± 0.023	this study
WISE 4.6 μm (mag)	11.612 ± 0.022	this study	8.537 ± 0.021	this study
WISE 12 μm (mag)	6.888 ± 0.015	this study	3.232 ± 0.012	this study
WISE 22 μm (mag)	2.657 ± 0.016	this study	−0.615 ± 0.014	this study
MSX 8.28 μm (Jy)	...	...	0.804 ± 0.130	Egan et al. (2003)
MSX 12.13 μm (Jy)	...	...	2.264 ± 0.134	Egan et al. (2003)
MSX 14.65 μm (Jy)	...	...	4.498 ± 0.279	Egan et al. (2003)
MSX 21.3 μm (Jy)	...	...	12.53 ± 0.764	Egan et al. (2003)
IRAS 12 μm <sup>a</sup> (Jy)	<0.47	Tajitsu & Tamura (1998)	2.08 ± 0.11	Tajitsu & Tamura (1998)
IRAS 25 μm (Jy)	0.83	Tajitsu & Tamura (1998)	19.09 ± 0.76	Tajitsu & Tamura (1998)
IRAS 60 μm (Jy)	1.27	Tajitsu & Tamura (1998)	11.11 ± 1.78	Tajitsu & Tamura (1998)
IRAS 100 μm <sup>a</sup> (Jy)	<18.17	Tajitsu & Tamura (1998)	8.08 ± 3.38	Tajitsu & Tamura (1998)
AKARI 9 μm (Jy)	...	...	0.846 ± 0.013	Yamamura et al. (2010)
AKARI 18 μm (Jy)	0.455 ± 0.035	Yamamura et al. (2010)	8.744 ± 0.088	Yamamura et al. (2010)
AKARI 65 μm <sup>b</sup> (Jy)	1.124:	Yamamura et al. (2010)	8.965 ± 1.050	Yamamura et al. (2010)
AKARI 90 μm (Jy)	0.807 ± 0.163	Yamamura et al. (2010)	8.009 ± 0.356	Yamamura et al. (2010)
AKARI 140 μm (Jy)	...	...	7.825 ± 3.180	Yamamura et al. (2010)
AKARI 160 μm <sup>b</sup> (Jy)	0.634:	Yamamura et al. (2010)	3.319:	Yamamura et al. (2010)
Free-free emission				
20 GHz (mJy)	...	...	105 ± 5	Mahony et al. (2011)
8.4 GHz (mJy)	...	...	111 ± 11	McConnell et al. (2012)
8.4 GHz (mJy)	...	...	99 ± 5	Mahony et al. (2011)
5 GHz (mJy)	3.0 ± 0.5	Stanghellini et al. (2008)	...	...
5 GHz (mJy)	<10	Milne & Aller (1982)	...	...
4.8 GHz (mJy)	...	...	112 ± 7	McConnell et al. (2012)
4.8 GHz (mJy)	...	...	116 ± 6	Mahony et al. (2011)
0.8 GHz (mJy)	...	...	42.7 ± 8.5	Mahony et al. (2011)

**Notes.**

<sup>a</sup> Note that some IRAS measurements at 12 and 100 μm denote upper limit results.

<sup>b</sup> Unreliable detections are marked with the colons.

$c - c'$ ,  $b - b'$ , and  $a - a'$  are 46°, 68°, and 72°. On this basis, through the observed structures from the HST images, we consider that not all lobes seen in Hen 2-158 and Pe 1-1 show a shell-like appearance (see Figure 1). For Hen 2-158, lobe  $c - c'$  is not obvious and does not show a shell-like structure, hence this feature is assigned a radially decreasing density distribution (Ueta et al. 2005). Since the boundary of lobe  $c - c'$  is not

apparent and this lobe is mostly overlapped with primary lobe  $d - d'$  in YPN Pe 1-1, the structure can also be reproduced using a uniform density distribution. With such a setup, we can see that the projected appearances created by these two models can basically match with the observed structures. The measured and simulated parameters of these lobes are given in Table 5.

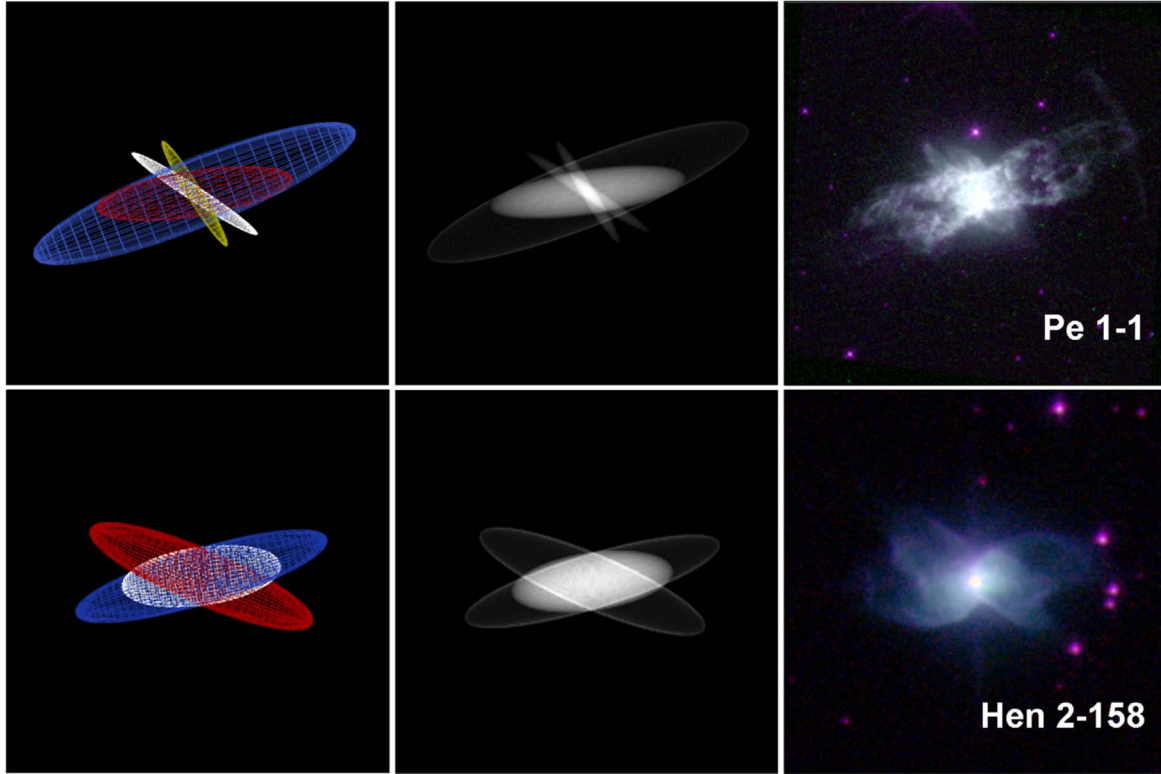


**Figure 8.** Comparison of simulated 3D models of two young PNs (Hen 2-158 and Pe 1-1) and their observed HST images. Left panels: 3D mesh models of Hen 2-158 and Pe 1-1. The outer arc-like structure is not made in the model of Pe 1-1. Middle panels: The rendered images of mesh models. Right panels: Observed HST color-composite images of these nebulae.

**Table 5**  
Modeling and Observed Parameters of the Lobes for Two Young PNs

Hen 2-158							
Feature	Observed			Density Distribution	Model		
	PA <sup>a</sup> (°)	Size ( $l'' \times w''$ )	Inclination <sup>b</sup> (°)		PA <sup>a</sup> (°)	Size ( $l'' \times w''$ )	Inclination <sup>b</sup> (°)
Lobe $a - a'$	$58 \pm 3$	$4.44 \times 0.88$	...	Shell	56	$5.53 \times 1.02$	36
Lobe $b - b'$	$105 \pm 4$	$5.51 \times 1.24$	...	Shell	104	$5.53 \times 1.16$	0
Lobe $c - c'$	$113 \pm 3$	$2.24 \times 1.17$	...	Uniform	115	$5.53 \times 1.16$	66
Pe 1-1							
Feature	Observed			Density Distribution	Model		
	PA <sup>a</sup> (°)	Size ( $l'' \times w''$ )	Inclination <sup>b</sup> (°)		PA <sup>a</sup> (°)	Size ( $l'' \times w''$ )	Inclination <sup>b</sup> (°)
Lobe $a - a'$	$34 \pm 4$	$5.68 \times 0.75$	...	Shell	34	$17.34 \times 1.71$	$72^d$
Lobe $b - b'$	$48 \pm 2$	$6.77 \times 0.77$	...	Shell	48	$17.34 \times 1.71$	$68^d$
Lobe $c - c'$	$101 \pm 3$	$12.72 \times 2.55$	...	Uniform	101	$17.34 \times 2.76$	$46^d$
Lobe $d - d'$	$112 \pm 4$	$17.62 \times 3.13$	$15^c$	Shell	112	$17.34 \times 3.13$	15

**Notes.**

<sup>a</sup> Referenced to major axes of individual lobes.

<sup>b</sup> Referenced to the plane of the sky (orientation of sky plane is  $0^\circ$ ).

<sup>c</sup> From Danehkar (2022).

<sup>d</sup> Derived based on the lobe  $d - d'$ .

Figure 8 shows a comparison of the constructed models for these two nebulae and the observed HST images. As can be seen from the rendered results shown in Figure 8, our two models present good approximations compared to our observations (middle panels of Figure 8). The 2D rendering results produced from the 3D models provide a good opportunity for us to study their complex structures of studied nebulae. In this study, although we attempted to construct the 3D models for the nebulae of interest based on their observed images, various 3D models may lead to 2D imaging results with similar appearances due to the projection effects (Chong et al. 2012). It is possible that the constructed 3D models of these PNs can be present in other nebulae, suggesting that multipolar nebulae may be more numerous than we thought and are common in young PNs. Here, our proposed models simply provide a morphological possibility for Hen 2-158 and Pe 1-1, which may cause some observational degeneracy and deficiencies. Further data obtained from integral-field spectrograph mounted on large telescopes are needed to help us to correct these shortcomings.

## 6. Discussion

From previous observations, more than half of the YPN population ( $\sim 57\%$ ) displayed bipolar, collimated-lobe, and multipolar structures (Sahai et al. 2011). The presence of these features suggests the formation of fast, highly collimated outflows ejected in various directions during the early stages of the PNs. To date, the true physical mechanism responsible for shaping multipolar PNs is still unclear. The multi-lobe structures can be (i) the result of multiple stellar winds with directional and temporal changes (typical multipolar PNs), which may involve the precessions caused by sub-stellar companions and/or a binary interactions (Class I objects, Hsia et al. 2014), (ii) produced by several episodic, collimated ejections originated from central binaries (nested PNs, Hsia et al. 2021) or multiple ionization layers with time variations extended along almost the same orientation, which are classified as Class II nebulae described by Hsia et al. (2014). Nested PNs can therefore be considered as non-typical multipolar nebulae.

Both of these objects (Hen 2-158 and Pe 1-1) display a similar appearance to other multipolar YPNs, whose nebulae show a well-defined multiple-lobe shape. It would be worth to study the possible correlation between typical multipolar YPNs (Class I objects) and young nested nebulae (Class II sources) by a statistical investigation for a sample of these nebulae. In order to accomplish this investigation, we have collected a sample of 56 nebulae reported in the literature that are found to reveal complex multipolar structures and nested shells (Manchado et al. 1996; López et al. 1998; Sahai et al. 2000; Sahai 2000; Kwok & Su 2005; Mampaso et al. 2006; Vázquez et al. 2008; Hsia et al. 2010; Kwok et al. 2010; Sahai et al.

2011; Clark et al. 2013; Guerrero et al. 2013; Guillén et al. 2013; Hsia et al. 2014; Rubio et al. 2015; Hsia et al. 2019, 2021) as summarized in Table 6.

From Table 6, we can see that a large proportion of studied objects ( $\sim 79\%$ ) reveals a typical multipolar appearance, and 12 out of 56 nebulae ( $\sim 21\%$ ) in our list show nested structures. These results suggest that typical multipolar YPNs appear more frequently than young nested nebulae. In addition, the largest PA difference between the lobes of 12 nested nebulae (see Table 6) is found to be no more than  $10^\circ$ . Assuming the number distribution of PA difference between the lobes for all 56 nebulae as a function of the normal distribution and the largest PA difference of nested nebular lobes less than  $10^\circ$ , the typical multipolar YPNs (Class I objects) are expected to account for the vast majority ( $>95\%$ ) of all nebulae in our sample. However, the expected proportion of typical multipolar YPN is larger than observed. Possible explanations are that many typical multipolar YPNs are misclassified into other morphological classes (Hsia et al. 2014) or these nebulae remain undiscovered due to poor dynamic-range observations and/or low-resolution imaging. Through further James Webb Space Telescope (JWST) observations, it is believed that more YPNs with a typical multipolar appearance can be discovered.

## 7. Conclusion

A series of recent studies aimed at young multipolar PNs (Sahai 2000; Hsia et al. 2010; Sahai et al. 2011; Chong et al. 2012; Clark et al. 2013; Hsia et al. 2014, 2019) have shown that these objects play a key role in PN morphological transition issue for low- to intermediate-mass stars evolved from AGB phase to PN stage. For a long time, multipolar nebulae as a member of YPNs are misclassified as elliptical and/or bipolar nebulae due to low-resolution and/or low-dynamic-range observations. Although an increasing number of nebulae with a multi-lobed appearance have been discovered through high-resolution HST observations, the true physical mechanism that causes these objects to take on their multipolar shapes remains unclear.

In this paper, we performed an optical morphological and infrared spectral study for two young PNs (Hen 2-158 and Pe 1-1) to understand their complex shapes and dust properties. HST optical images of these nebulae reveal that they both have several bipolar lobes, and an arc-shaped filament with a clear boundary is located at the northwestern side of Pe 1-1. The appearance of this arc-like feature suggests that this nebula interacts with its surrounding ISM. We also studied the dust properties of these two multipolar PNs through their infrared spectra. The Spitzer IRS spectroscopic observations of these young nebulae clearly show the prominent UIE features at 6.2, 7.7, 8.6, 11.2, 12.0, 12.8, 16.4, 16.7, and  $17.0 \mu\text{m}$ . A weak crystalline silicate feature at  $13.58 \mu\text{m}$  is detected in Pe 1-1. These features reveal a carbon-rich dust characteristic in Hen

**Table 6**  
Properties of Typical Multipolar YPNs and Young Nested Nebulae

PN Name	PA of Lobe ( $^{\circ}$ )	Reference	PN Name	PA of Lobe ( $^{\circ}$ )	References
Typical Multipolar YPNs (Class I objects) <sup>a</sup>					
G 002.1–04.2	2, 8, 134, 154	Hsia et al. (2014)	G 002.6–03.4	...	Sahai et al. (2011)
G 003.1+02.9	...	Sahai et al. (2011)	G 003.6+06.1	–84, 7, 26	Chong et al. (2012)
G 006.4+02.0	...	Sahai et al. (2011)	G 008.3–07.3	–27, –43	Hsia et al. (2010)
G 009.6+14.8	40, 72	Rubio et al. (2015)	G 019.4–05.3	34, 122, 149, 162	Hsia et al. (2014)
G 021.8–00.4	...	Manchado et al. (1996)	G 023.9–02.3	15, 120, 130	Hsia et al. (2014)
G 024.8–02.7	15, 40	Manchado et al. (1996)	G 027.6–09.6	...	Sahai et al. (2011)
G 037.8–06.3	118, 119, 133	Hsia et al. (2014)	G 043.0–03.0	45, 90	Manchado et al. (1996)
G 048.7+02.3	–20, 100	Manchado et al. (1996)	G 057.9–01.5	44, 65	Hsia et al. (2014)
G 064.6+48.2	–32, –52, 7	Guillén et al. (2013)	G 068.8–00.0	–30, 10	Manchado et al. (1996)
G 071.6–02.3	58, 60, 170, 172	Hsia et al. (2014)	G 071.6–02.3	...	Sahai et al. (2011)
G 074.5+02.1	132, 148	Kwok & Su (2005)	G 082.1+07.0	...	Sahai et al. (2011)
G 084.7–08.0	65, 110	Guerrero et al. (2013)	G 089.0+00.3	...	Clark et al. (2013)
G 089.8–05.1	88, 115	Hsia et al. (2014)	G 093.9–00.1	13, 35, 139	Hsia et al. (2019)
G 100.0–08.7	...	Sahai et al. (2011)	G 126.6+01.3	...	Mampaso et al. (2006)
G 234.8+02.4	35, 60, 85	López et al. (1998)	G 285.4+01.5	34, 48, 101, 112	This study
G 285.6–02.7	...	Sahai et al. (2011)	G 307.2–03.4	10, 37, 90, 141	Sabin et al. (2012)
G 309.1–04.3	...	Hsia et al. (2019)	G 320.1–09.6	...	Sahai et al. (2011)
G 321.0+03.9	...	Sahai et al. (2011)	G 327.8–06.1	58, 105, 113	This study
G 332.9–09.9	...	Sahai et al. (2011)	G 342.1+10.8	...	Kwok et al. (2010)
G 352.6+03.0	...	Sahai et al. (2011)	G 355.9–04.2	78, 129	Hsia et al. (2014)
G 358.5–04.2	...	Sahai et al. (2011)	G 358.9+03.4	...	Sahai et al. (2011)
G 358.9–00.7	...	Sahai et al. (2011)	G 359.3–00.9	...	Hsia et al. (2019)
Young Nested PNs (Class II objects) <sup>a</sup>					
G 010.8+18.0	...	Hsia et al. (2021)	G 061.3+03.6	...	Hsia et al. (2021)
G 068.1+11.0	...	Hsia et al. (2021)	G 086.5–08.8	...	Hsia et al. (2021)
G 086.9–03.4	...	Hsia et al. (2021)	G 111.8–02.8	–7, –7, –9	Hsia et al. (2021)
G 300.7–02.0	46, 49	Hsia et al. (2014, 2021)	G 307.5–04.9	...	Hsia et al. (2021)
G 315.4+09.4	...	Hsia et al. (2021)	G 331.7–01.0	...	Hsia et al. (2021)
G 352.9–07.5	75, 79, 80, 81	Hsia et al. (2014, 2021)	PN M 2–56	...	Hsia et al. (2021)

**Note.**

<sup>a</sup> According to the classification described by Hsia et al. (2014).

2-158 and a mixed chemistry environment in Pe 1-1, which may dabble in carbon-rich dust mass-loss processes originated from the massive progenitors of YPNs.

From the analyses of the SED fitting curves for Hen 2-158 and Pe 1-1, we found that these PNs both show low luminosities and low effective temperatures of their exciting sources. These results suggest that these nebulae are young PNs and their evolutionary ages are small. Furthermore, we construct two 3D models for the young PNs with multiple lobes to realize and understand their intrinsic structures using the *ShapeX* software package. These simulated results of the nebulae suggest that multipolar nebulae may be more numerous than we thought and probably they are common in young PNs.

A large fraction of 56 studied nebulae ( $\sim 79\%$ ) is found to show a typical multipolar appearance, which is lower than the expected fraction ( $>95\%$ ). This may be due to poor

observations, and possibly further high-resolution measurements could help us to learn more about these objects.

Young PNs are thought to be an evolutionary transition between post-AGB stage and PN phase. The existence of multipolar nebulae may be only the tip of the iceberg among the young PNs. With the advancement of astronomical technology, it is believed that more multi-lobed objects will be discovered. Probably further JWST measurements can help us to clarify these issues.

**Acknowledgments**

We would like to thank the anonymous referee for his/her helpful comments that improved the manuscript. Part of the data used in this study were obtained from the Multi-mission Archive at the Space Telescope Science Institute (MAST). STScI is operated by the Association of Universities for

Research in Astronomy, Inc., under NASA contract NAS5-26555. Support for MAST for non-HST data is provided by the NASA Office of Space Science via grant NAG5-7584 and by other grants and contracts. The Laboratory for Space Research was established by a grant from the University Development Fund of the University of Hong Kong. C.-H.H. thanks supports from the Hong Kong Research Grants Council for GRF research support under the grants 17326 116 and 17300417. C.-H.H. thanks Q.A. Parker and HKU for provision of his research post.

## ORCID iDs

Chih-Hao Hsia  <https://orcid.org/0000-0003-2549-3326>

## References

- Acker, A., Gesicki, K., Grosdidier, Y., & Durand, S. 2002, *A&A*, **384**, 620
- Ali, A., Sabin, L., Snaid, S., & Basurah, H. M. 2012, *A&A*, **541**, A98
- Burlak, M. A., & Kniazev, A. Y. 2013, *AstL*, **39**, 703
- Chabrier, G. 2003, *PASP*, **115**, 809
- Chong, S.-N., Kwork, S., Imai, H., et al. 2012, *ApJ*, **160**, 115
- Clark, D. M., López, J. A., Steffen, W., et al. 2013, *AJ*, **145**, 57
- Coccatto, L., Gerhard, O., Arnaboldi, M., et al. 2009, *MNRAS*, **394**, 3
- Corradi, R. L. M., Schönberner, D., Steffen, M., et al. 2003, *MNRAS*, **340**, 417
- Cutri, R. M., Skrutskie, M. F., van Dyk, S., et al. 2003, *yCat*, **II/246**
- Danehar, A. 2022, *ApJS*, **260**, 14
- Delgado-Inglada, G. 2017, in *Planetary Nebulae: Multi-Wavelength Probes of Stellar and Galactic Evolution*, Proc. IAU Symp., 323, ed. X. Liu, L. Stanghellini, & A. Karakas, 51
- Dgani, R., & Soker, N. 1998, *ApJ*, **495**, 337
- Egan, M. P., Price, S. D., Kraemer, K. E., et al. 2003, *The Midcourse Space Experiment Point Source Catalogue v2.3*, Air Research Laboratory Technical Report AFRL-VS-TR-2003-1589
- Guerrero, M. A., & Machado, A. 1998, *ApJ*, **508**, 262
- Guerrero, M. A., Miranda, L. F., Ramos-Larios, G., & Vázquez, R. 2013, *A&A*, **551**, 53
- Guillén, P. F., Vázquez, R., Miranda, L. F., et al. 2013, *MNRAS*, **432**, 2676
- Gussie, G. T., & Taylor, A. R. 1994, *PASP*, **106**, 500
- Henden, A. A., Templeton, M., Terrell, D., et al. 2016, *yCat*, **2336**, 0
- Henize, K. G. 1967, *ApJS*, **14**, 125
- Herrmann, K. A., Ciardullo, R., Feldmeier, J. J., & Vinciguerra, M. 2008, *AJ*, **683**, 2
- Higdon, S. J. U., Devost, D., Higdon, J. L., et al. 2004, *PASP*, **116**, 975
- Hsia, C.-H., Chau, W., Zhang, Y., & Kwok, S. 2014, *ApJ*, **787**, 25
- Hsia, C.-H., Kwok, S., Zhang, Y., et al. 2010, *ApJ*, **725**, 173
- Hsia, C.-H., & Zhang, Y. 2014, *A&A*, **563A**, 63
- Hsia, C.-H., Zhang, Y., Kwok, S., & Chau, W. 2019, *Astrophysics and Space Science*, **364**, 32
- Hsia, C.-H., Zhang, Y., Sadjadi, S., et al. 2021, *A&A*, **655**, A46
- Hsia, C.-H., Zhang, Y., Zhang, X.-L., & Luo, T. 2020, *RAA*, **20**, 107
- Ivezic, Z., Nenkova, M., & Elitzur, M. 1999, *DUSTY User Manual Internal Report* University of Kentucky
- Jacoby, G. H., Ferland, G. J., & Korista, K. T. 2001, *ApJ*, **560**, 272
- Kwok, S. 2000, *The Origin and Evolution of Planetary Nebulae* (New York: Cambridge Astrophysics Series), 33
- Kwok, S., Chong, S.-N., Hsia, C.-H., et al. 2010, *ApJ*, **708**, 93
- Kwok, S., & Su, K. Y. L. 2005, *ApJ*, **635**, 49
- López, J. A., Meaburn, J., Bryce, M., et al. 1998, *ApJ*, **493**, 803
- Mahony, E. K., Sadler, E. M., Croom, S. M., et al. 2011, *MNRAS*, **417**, 2651
- Mampaso, A., Corradi, R. L. M., Viironen, K., et al. 2006, *A&A*, **458**, 203
- Manchado, A., Stanghellini, L., & Guerrero, M. A. 1996, *ApJ*, **466**, 95
- Marocco, F., Eisenhardt, P. R. M., Fowler, J. W., et al. 2021, *ApJS*, **253**, 8
- Mathis, J. S., Ruml, W., & Nordsieck, K. H. 1977, *ApJ*, **217**, 425
- McConnell, D., Sadler, E. M., Murphy, T., & Ekers, R. D. 2012, *MNRAS*, **422**, 1527
- Merrett, H. R., Merrifield, M. R., Douglas, N. G., et al. 2006, *MNRAS*, **369**, 1
- Milne, D. K., & Aller, L. H. 1982, *A&AS*, **50**, 209
- Molster, F. J., Waters, L. B. F. M., & Tielens, A. G. G. M. 2002, *A&A*, **382**, 222
- Moreno-Ibáñez, M., Villaver, E., Shaw, R. A., & Stanghellini, L. 2016, *A&A*, **593**, A29
- Parker, Q. A., Bojičić, I., & Frew, D. J. 2017, in *IAU Symp. 323, Planetary Nebulae: Multi-Wavelength Probes of Stellar and Galactic Evolution*, ed. X. Liu, L. Stanghellini, & A. Karakas (Cambridge: Cambridge Univ. Press), 36
- Peña, M., Ruiz-Escobedo, F., Rechy-García, J. S., & García-Rojas, J. 2017, *MNRAS*, **472**, 1182
- Perek, L. 1960, *BAICZ*, **11**, 256
- Phillips, J. P. 2004, *MNRAS*, **353**, 589
- Quireza, C., Rocha-Pinto, H. J., & Maciel, W. J. 2007, *A&A*, **475**, 217
- Ramos-Larios, G., Guerrero, M. A., Nigoche-Netro, A., et al. 2018, *MNRAS*, **475**, 932
- Rubio, G., Vázquez, R., Ramos-Larios, G., et al. 2015, *MNRAS*, **446**, 1931
- Sabin, L., Vázquez, R., López, J. A., et al. 2012, *RMxAA*, **48**, 165
- Sahai, R. 2000, *ApJL*, **537**, 43
- Sahai, R., Morris, M. R., & Villar, G. G. 2011, *AJ*, **141**, 134
- Sahai, R., Nyman, L., & Nyman, L.-Å. 2000, *ApJ*, **543**, 880
- Santander-García, M., Rodríguez-Gil, P., Hernandez, O., et al. 2010, *A&A*, **519**, A54
- Stanghellini, L., García-Hernández, D. A., García-Lario, P., et al. 2012, *ApJ*, **753**, 172
- Stanghellini, L., Shaw, R. A., & Villaver, E. 2008, *ApJ*, **689**, 194
- Stanghellini, L., Shaw, R. A., & Villaver, E. 2016, *ApJ*, **830**, 33
- Steffen, W., Koning, N., Wenger, S., Morisset, C., & Magnor, M. 2011, *IEEE Trans. Vis. Comput. Graphics*, **17**, 454
- Tajitsu, A., & Tamura, S. 1998, *AJ*, **115**, 1989
- Tylenda, R., Siódmiak, N., Górný, S. K., et al. 2003, *A&A*, **405**, 627
- Ueta, T., Murakawa, K., & Meixner, M. 2005, *AJ*, **129**, 1625
- Vázquez, R., Miranda, L. F., Olguín, L., et al. 2008, *A&A*, **481**, 107
- Wareing, C. J., Zijlstra, A. A., & O'Brien, T. J. 2007, *MNRAS*, **382**, 1233
- Weidmann, W. A., Mari, M. B., Schmidt, E. O., et al. 2020, *A&A*, **640**, A10
- Weinberger, R. 1989, *A&AS*, **78**, 301
- Wright, E. L., Eisenhardt, P. R. M., Mainzer, A. K., et al. 2010, *AJ*, **140**, 1868
- Yamamura, I., Makiuti, S., Ikeda, N., et al. 2010, *yCat*, **2298**, 0